Nuclear Technology

ISSN: (Print) (Online) Journal homepage: https://www.tandfonline.com/loi/unct20

Enhancing the One-Dimensional SFR Thermal Stratification Model via Advanced Inverse Uncertainty Quantification Methods

Cihang Lu , Zeyun Wu & Xu Wu

To cite this article: Cihang Lu , Zeyun Wu & Xu Wu (2020): Enhancing the One-Dimensional SFR Thermal Stratification Model via Advanced Inverse Uncertainty Quantification Methods, Nuclear Technology, DOI: 10.1080/00295450.2020.1805259

To link to this article: https://doi.org/10.1080/00295450.2020.1805259

Published online: 16 Oct 2020.

NUCLEAR TECHNOLOGY

DOI: https://doi.org/10.1080/00295450.2020.1805259

Enhancing the One-Dimensional SFR Thermal Stratification Model via Advanced Inverse Uncertainty Quantification Methods

Cihang Lu,[a] Zeyun Wu,[a]* and Xu Wu[b]

[a]Virginia Commonwealth University, Department of Mechanical and Nuclear Engineering, Richmond, Virginia 23219
[b]North Carolina State University, Department of Nuclear Engineering, Raleigh, North Carolina 27695

Received April 27, 2020
Accepted for Publication July 28, 2020

Abstract — *Thermal stratification (TS) is a thermal-fluid phenomenon that can introduce large uncertainties to nuclear reactor safety. The stratified layers caused by TS can lead to temperature oscillations in the reactor core. They can also result in damages to both the reactor vessel and in-vessel components due to the growth of thermal fatigue cracks. More importantly, TS can impede the establishment of natural circulation, which is widely used for passive cooling and ensures the inherent safety of numerous reactor designs. A fast-running one-dimensional (1-D) model was recently developed in our research group to predict the TS phenomenon in pool-type sodium-cooled fast reactors. The efficient 1-D model provided reasonable temperature predictions for the test conditions investigated, but nonnegligible discrepancies between the 1-D predictions and the experimental temperature measurements were observed. These discrepancies are attributed to the model uncertainties (also known as model bias or errors) in the 1-D model and the parameter uncertainties in the input parameters.*

In this study, we first recognized through a forward uncertainty analysis that the observed discrepancies between the computational predictions and the experimental temperature measurements could not be explained solely by input uncertainty propagation. We then performed an inverse uncertainty quantification (UQ) study to reduce the model uncertainties of the 1-D model using a modular Bayesian approach based on experimental data. Inverse UQ serves as a data assimilation process to simultaneously minimize the mismatches between the predictions and experimental measurements, while quantifying the associated parameter uncertainties. The solutions of the modular Bayesian approach were in the form of posterior probability density functions, which were explored by rigorous Markov Chain Monte Carlo sampling. Results showed that the quantified parameters obtained from the inverse UQ effectively improved the predictive capability of the 1-D TS model.

Keywords — *Thermal stratification, sodium-cooled fast reactor, sensitivity analysis, inverse uncertainty quantification.*

Note — *Some figures may be in color only in the electronic version.*

I. INTRODUCTION

Thermal stratification is an important phenomenon that can take place in many components of nuclear power plants, such as the plena of the liquid-metal-cooled reactors and the piping systems of the water-cooled reactors. This phenomenon can be established during different transients of a reactor with power changes when coolant jets enter an enclosure filled with an ambient fluid with a different temperature. For example, thermal-stratified layers of liquid sodium with a large vertical temperature gradient could be established in the upper plenum of a sodium-cooled faster reactor (SFR)

*E-mail: zwu@vcu.edu

during both protected loss-of-flow transients with scram and unprotected loss-of-flow accidents without scram.[1] Thermal stratification introduces uncertainties to core safety because the thermal-stratified layers can lead to temperature oscillations in the reactor core.[2] Thermal stratification can also result in damages to both the reactor vessel and in-vessel components due to thermal fatigue crack growth.[3] More importantly, thermal stratification can impede the establishment of natural circulation,[4] which is widely used for passive cooling and ensures the inherent safety of numerous reactor designs, including pool-type SFRs, high-temperature gas-cooled reactors, and small modular boiling water reactors.

Many computational efforts have been made to predict the thermal stratification phenomenon with different fidelities to prevent its occurrence or to mitigate the damage caused. Several system-level codes are capable of predicting the thermal stratification phenomenon at a low computational cost,[5–7] but can only provide approximated solutions for simple cases. Computational fluid dynamics (CFD) modeling, on the contrary, gives accurate calculations of thermal stratification.[8–10] However, the CFD calculations are computationally expensive and time consuming, and are not suitable when a large number of transient calculations are needed for core safety analysis. In our previous publication,[11,12] we developed a fast-running one-dimensional (1-D) system-level model to predict thermal stratification phenomenon in the upper plenum of a pool-type SFR, which is desirable when numerous transient calculations are to be performed. Our 1-D model showed similar performance with that of the CFD model for the cases that we studied, but nonnegligible discrepancies between the 1-D predictions and the experimental temperature measurements were observed.[11] It is pointed out that while the discrepancy between 1-D calculations and experimental temperature measurements was considered as the figure of merit in terms of the prediction of thermal stratification, more proper metrics may exist when the prediction of natural circulation is focused.

Continuing with previous research efforts, we improved the 1-D thermal stratification model in this work, seeking a better understanding of the discrepancies between the predictions and measurements. We first performed a forward uncertainty analysis and determined that the observed discrepancies between the 1-D predictions and the experimental measurements could not be explained solely by input uncertainty propagation, whereas the model uncertainties (also known as model bias or errors) associated with the 1-D model also needed to be considered. We then improved the 1-D model by determining the optimum parameters to be used for the correlation of the turbulence-enhanced sodium thermal conductivity through an inverse uncertainty quantification (UQ) analysis, which has been widely used in the literature for the calibration of thermal-hydraulic parameters.[13,14] We used the Markov Chain Monte Carlo (MCMC) sampling method to explore the posterior probability density functions (PDFs) generated from the Bayesian-theory-based inverse UQ process employed. Instead of simply determining the point estimates of the parameters that minimize the mismatches between the predictions and experimental data, the inverse UQ process used in the current study also quantified the uncertainties associated with the estimations.

The rest of this paper is organized as follows. In Sec. II, the test conditions used for the inverse UQ process are summarized. The apparatus, in which the experimental data were obtained, is briefly introduced in this section as well. The 1-D model is also presented to emphasize the terms to be improved. In Sec. III, a tentative forward UQ analysis is conducted with the intention of determining whether the observed discrepancies between the 1-D predictions and the experimental measurements could be explained solely by input uncertainty propagation, and also to identify possible terms needing improvement in the 1-D model. In Sec. IV, an inverse UQ analysis is performed to develop a better correlation for the turbulence-enhanced sodium thermal conductivity that improves the 1-D predictions. In Sec. V, the work accomplished in this study is summarized, and some future research directions in this regard are envisioned.

II. EXPERIMENT CONFIGURATION AND COMPUTATIONAL MODEL

II.A. Experimental Configuration

The experimental data used for the validation of the 1-D thermal stratification model were obtained in the Thermal Stratification Experimental Facility (TSTF) developed at the University of Wisconsin-Madison.[15] A diagram of the test section of the TSTF is shown in Fig. 1.

During an experimental test, sodium jets were injected from the bottom portion of the TSTF into the test section to mimic the impinging jets flowing into the upper plenum of an SFR. Only the cases where jets with lower temperatures enter a tank filled with higher-temperature fluid were considered in the experiments at this moment. Two subcases were further considered. In subcase I, an upper instrumentation structure (UIS) was installed in the tank (see Fig. 1) to

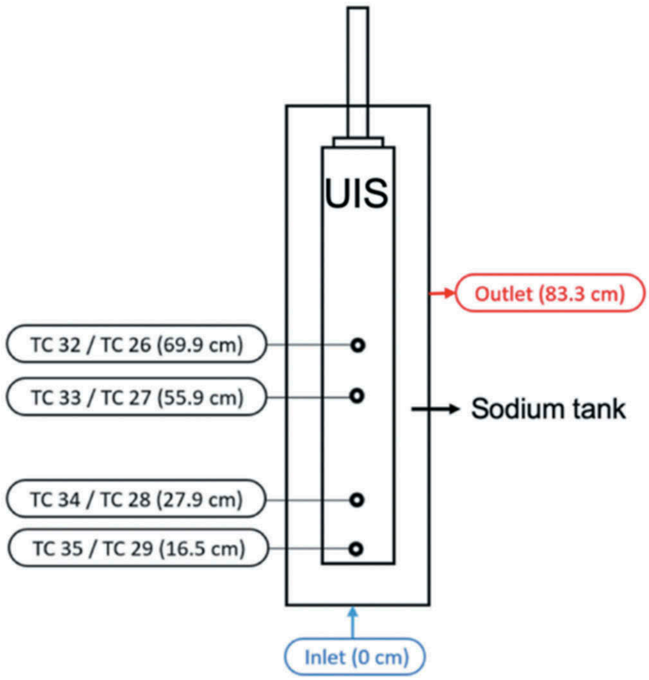

Fig. 1. Test section of the TSTF with TCs and outlet positioned.

emulate the in-vessel components located in the upper plenum of an SFR that block the inlet of the impinging jets. In subcase II, no UIS was installed. The temperature measurements were continuously collected at four different axial locations during the experiments, as indicated by the thermocouple (TC) positions in Fig. 1. Two TCs measured the temperature of the ambient fluid in the tank simultaneously at the same axial location. The experiments were conducted under nine test conditions, with three corresponding to subcase I and the others corresponding to subcase II. The test conditions of the experiments are summarized in Table I. All experimental data were compiled in an Excel file for further investigations.

II.B. One-Dimensional Thermal Stratification Model

Equation (1), which describes the temperature field model used in our previous studies[11,12] to predict the temperature profile of the ambient fluid in the sodium tank, essentially represents the energy conservation of the sodium after incorporating the mass continuum principle:

$$\rho_{sf} c_{p,sf} \frac{\partial T_{sf}}{\partial t} + \rho_{sf} c_{p,sf} \frac{Q_{jet}}{A_{sf}} \frac{\partial T_{sf}}{\partial z} - \frac{\partial}{\partial z}\left(k_{sf} \frac{\partial T_{sf}}{\partial z}\right) = \frac{c_{p,jet}\rho_{jet}}{A_{sf}} Q'_{jet}\left(T_{jet} - T_{sf}\right) , \tag{1}$$

where

ρ_{sf} = mass density of the ambient fluid

$c_{p,sf}$ = heat capacity of the ambient fluid

A_{sf} = surface area of the ambient fluid

T_{sf} = temperature of the ambient fluid

ρ_{jet} = mass density of the impinging jet

$c_{p,jet}$ = heat capacity of the impinging jet

Q_{jet} = volumetric flow rate of the impinging jet

T_{jet} = temperature of the impinging jet

Q'_{jet} = volumetric dispersion rate of the impinging jet.

One unique feature of Eq. (1) is the use of integral techniques to convert the jets to heat source terms appearing on the right side of the diffusion convection.[7] In Eq. (1), k_{sf} is the thermal conductivity of the ambient fluid, which may differ from the static thermal conductivity k_c of the ambient fluid in different flow conditions. This is because the ambient fluid may become turbulent due to the dispersion of the impinging jets, and the heat transfer of the ambient fluid may be enhanced by the turbulence. In our previous publication, we used the correlation established by Shih et al.[16] to estimate the relation between the turbulence-enhanced

TABLE I

Test Conditions of the Experiments Performed

Test Number	Inlet Temperature (°C)	Initial Temperature (°C)	Flow Rate (gpm)	
1	200	250	6	With UIS
2	200	250	10	
3	200	225	10	
4	200	300	1.5	Without UIS
5	200	250	3	
6	200	300	3	
7	200	250	3.7	
8	200	300	10	
9	200	250	10	

thermal diffusivity α^{tot} and the static thermal diffusivity α_c by neglecting the impact of sodium mass density and heat capacity on its thermal diffusivity, and assumed the correlation between k_{sf} and k_c to be similar to that between α^{tot} and α_c. Shih et al. defined three mixing regimes according to the ratio of the turbulent Reynolds number Re_τ to the Richardson number Ri and established the empirical correlations between α^{tot} and α_c with different coefficients in each mixing regime, as summarized in Table II.

In Eq. (1), $Q_{jet}^{'}$ represents the linear volumetric dispersion rate of the impinging jet. It was assumed that the impinging jets uniformly dispersed in the ambient fluid within a length of L_{jet}, and

$$Q_{jet}^{'} = Q_{jet}/L_{jet} . \tag{2}$$

In subcase I, the jets hit the bottom of the UIS after entering the test section and were not able to rise above the UIS before dispersing in the ambient fluid. Therefore, we assumed that the impinging sodium was evenly dispersed in the ambient fluid within the distance between the bottom of the UIS and the jet inlet surface z_{UIS}, which was about 5 cm in the experiment, and $L_{jet} = z_{\mathrm{UIS}}$. In subcase II, the modeling of L_{jet} became more difficult due to the absence of the UIS. The correlation for the jet velocity was proposed to be

$$dv_{jet} = -\left(C\frac{v^2\rho_{sf}}{\rho_{jet}} + \frac{\rho_{jet}-\rho_{sf}}{\rho_{jet}}g_0\right)dt , \tag{3}$$

where v was the initial jet velocity, and g_0 was the standard acceleration due to gravity. The coefficient C was found to be 4.3 in our previous publication.[11]

III. FORWARD UQ ON THE IMPACT OF DIFFERENT PARAMETERS

This section presents the results from a preliminary forward UQ analysis. A sampling-based forward UQ approach was employed in this section. For each forward calculation (also known as realization), we simply varied one individual input parameter under investigation within a certain assumed uncertainty range and kept all other parameters unchanged. The uncertainties associated with the input parameter were determined by analyzing the statistical distributions of the outcomes. The intention of the forward UQ analysis was to determine if the observed discrepancies between the 1-D predictions and the experimental measurements could be explained solely by the input uncertainty propagation. The terms needing improvement in the 1-D thermal stratification model were also identified according to the forward UQ analysis.

III.A. Subcase I with UIS Installed

The test condition in test 1 in Table I was used for forward UQ analysis of subcase I with UIS installed. Figure 2 compares the 1-D model predictions to the average temperature measurement of the two TCs at each of the four axial locations in this test condition. The predicted temperature had a slight rise after 100 s of elapsed time because the inlet temperature was not perfectly controlled during the experiment and became slightly hotter than 200°C after the 100-s elapsed time.

To highlight the discrepancies, Fig. 3 illustrates the percentage differences of the predicted temperatures to the measurements along the elapsed time. Note the temperature percentage changes were calculated based on kelvins. As indicated in Fig. 3, the temperature difference calculated for TC 26/TC 32 at 175 s elapsed time had the largest discrepancy (~4.5%) with the measurements, thus this temperature was selected as the reference for the further uncertainty source investigation in the following steps.

The input parameters and the thermal-hydraulic system parameters considered to impact the thermal stratification phenomenon in this subcase included (1) jet volumetric flow rate, (2) jet temperature, (3) sodium heat capacity, and (4) sodium thermal conductivity.

TABLE II

Correlations between α^{tot} and α*

Regime	$\frac{\mathrm{Re}_\tau}{\mathrm{Ri}}$	α^{tot}
Molecular	$\frac{\mathrm{Re}_\tau}{\mathrm{Ri}} < 150$	α_c
Transitional	$150 < \frac{\mathrm{Re}_\tau}{\mathrm{Ri}} < 1000$	$0.015\frac{\mathrm{Re}_\tau}{\mathrm{Ri}} \cdot \alpha_c$
Energetic	$1000 < \frac{\mathrm{Re}_\tau}{\mathrm{Ri}}$	$0.015\left(\frac{\mathrm{Re}_\tau}{\mathrm{Ri}}\right)^{0.5} \cdot \alpha_c$

*Reference 16.

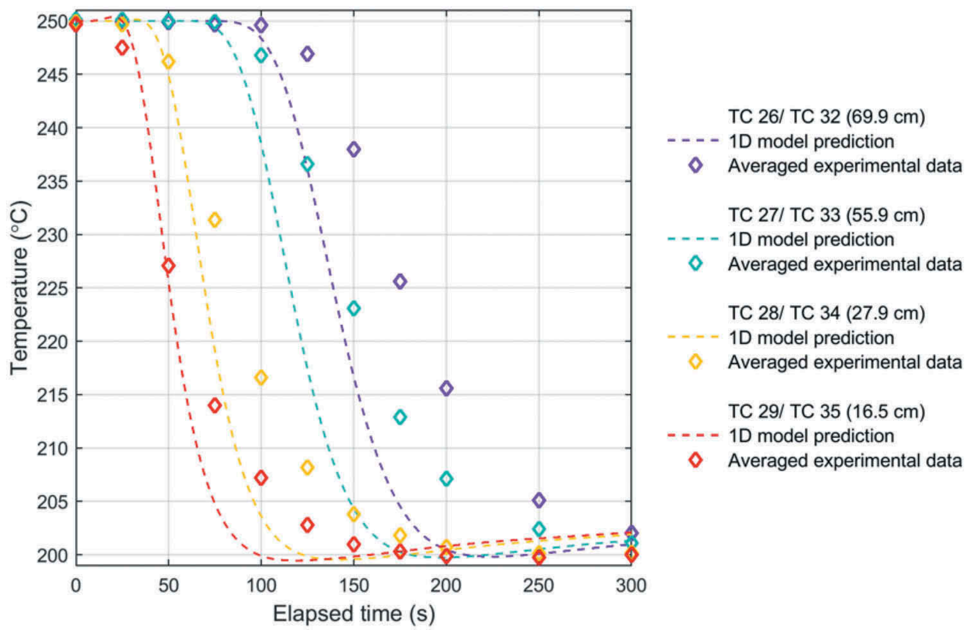

Fig. 2. Comparison of predictions with experiments in test 1.

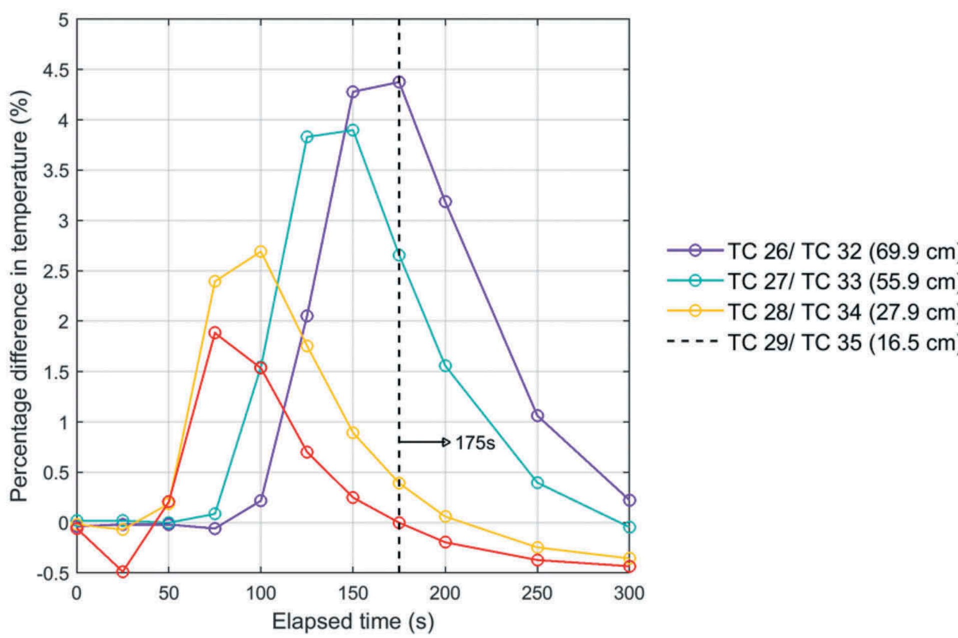

Fig. 3. Percentage difference between predictions and experiments in test 1.

Based on our knowledge of the precision of the measurement equipment employed in the experiment, the jet volumetric flow rate and jet temperature were varied uniformly between 97% and 103% of their reference values. Sodium heat capacity was varied uniformly between 97% and 103% of its reference value,[17] and sodium thermal conductivity was varied uniformly between 95% and 105% of its reference value.[17] The resultant ambient temperatures calculated for TC 26/TC 32 corresponding to various levels of variations to the reference jet volumetric flow rate are compared with the experimental data in Fig. 4, as an example.

The percentage change of the temperature calculated for TC 26/TC 32 at 175 s at various levels of changes for the four parameters considered are compared in Fig. 5. An uncertainty of ±3% in the calculation of the sodium heat capacity and of

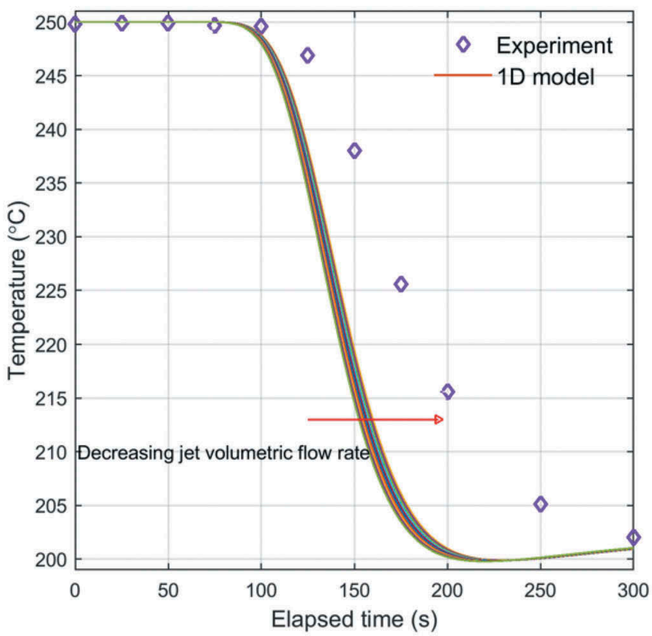

Fig. 4. Ambient temperature prediction at TC 26/TC 32 (69.9 cm) with various perturbed impinging jet flow rates in test 1.

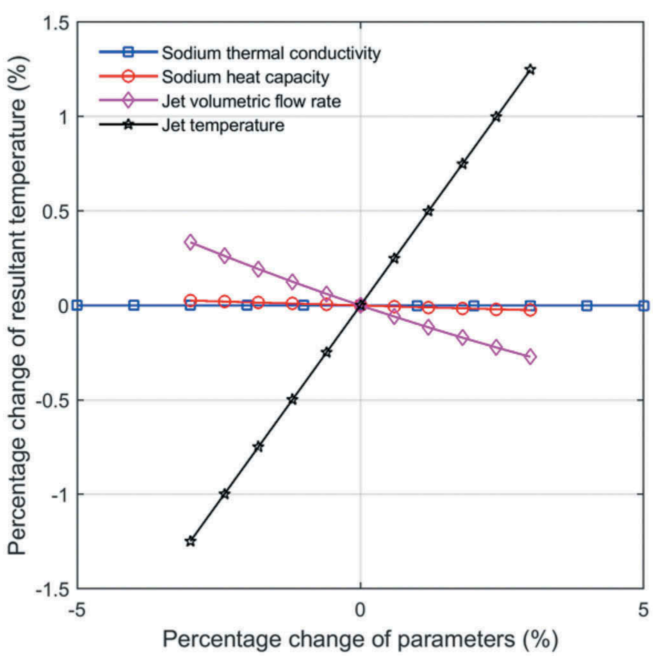

Fig. 5. Temperature percentage changes due to different parameters at 175 s in test 1.

±5% in the calculation of the sodium thermal conductivity had a negligible impact on the resultant temperature. However, the percentage changes of the temperature of interest due to the uncertainties of the inlet temperature (~1.2%) and the inlet volumetric flow rate (~0.4%) were more significant, and the uncertainties caused by the error propagation in the computational model were not enough to compensate for the temperature discrepancies between the 1-D predictions and the experimental measurements.

III.B. Subcase II with No UIS Installed

The test condition in test 4 in Table I was used for the forward UQ analysis for subcase II with no UIS installed. The 1-D predictions were compared with the average temperature measurement of the two TCs at each of the four axial locations, as shown in Fig. 6. The temperature calculated for TC 26/TC 32 at the 700-s elapsed time was selected to be the reference for the UQ because it had the largest discrepancy (~4.5%) with the measurements, as shown in Fig. 7.

In addition to the four parameters investigated in subcase I, the change in the temperature of interest induced by the uncertainty of coefficient C in Eq. (3) was also studied. Jet volumetric flow rate, jet temperature, and the coefficient C were varied uniformly between 97% and 103% of their reference values. Sodium heat capacity was varied uniformly between 97% and 103% of its reference value, and sodium thermal conductivity was varied uniformly between 95% and 105% of its reference value. The resultant ambient temperatures calculated for TC 26/TC 32 corresponding to various levels of variations to the reference jet volumetric flow rate are compared with the experimental data in Fig. 8, as an example.

The percentage change of the temperature calculated for TC 26/TC 32 at 700 s due to the five parameters selected are compared in Fig. 9. An uncertainty of ±3% in the sodium heat capacity and coefficient C and of ±5% in the sodium thermal conductivity had negligible impact on the resultant temperature. The percentage change of the temperature of interest was more significant due to the uncertainties of the inlet temperature (~0.9%) and the inlet volumetric flow rate (~0.5%), but was not enough to compensate for the temperature discrepancies between the experimental measurements and the 1-D predictions.

According to the forward UQ analysis for both subcases outlined previously, we recognized that the observed discrepancies between the 1-D predictions and the experimental measurements could not be explained solely by input uncertainty propagation. The discrepancies therefore are likely caused by other model deficiencies. The forward UQ analysis showed that an uncertainty of ±5% in sodium thermal conductivity had a negligible impact on the resultant temperature prediction. However, through the enhancement of turbulence, the sodium

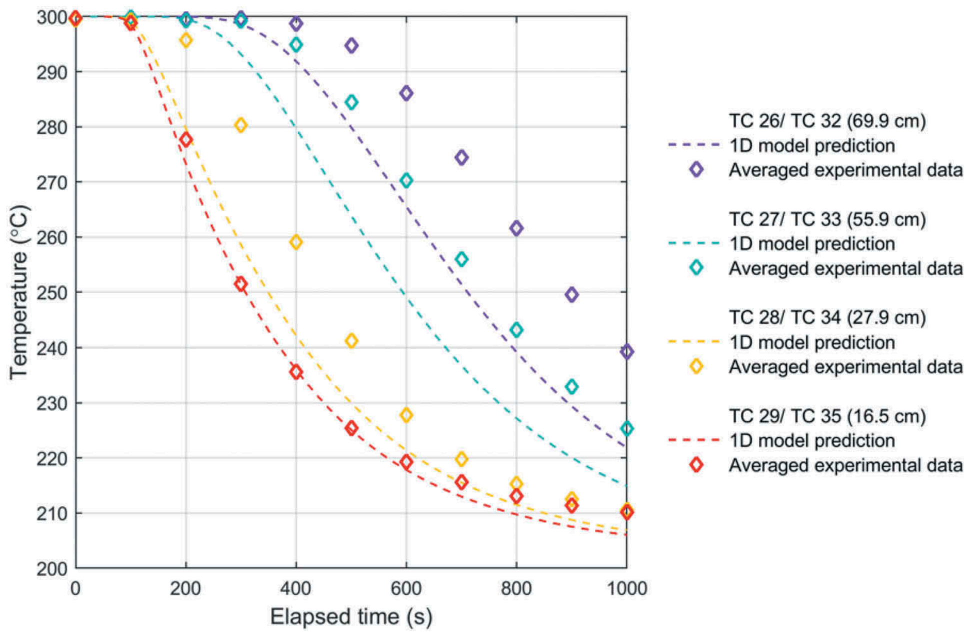

Fig. 6. Comparison of predictions with experiments in test 4.

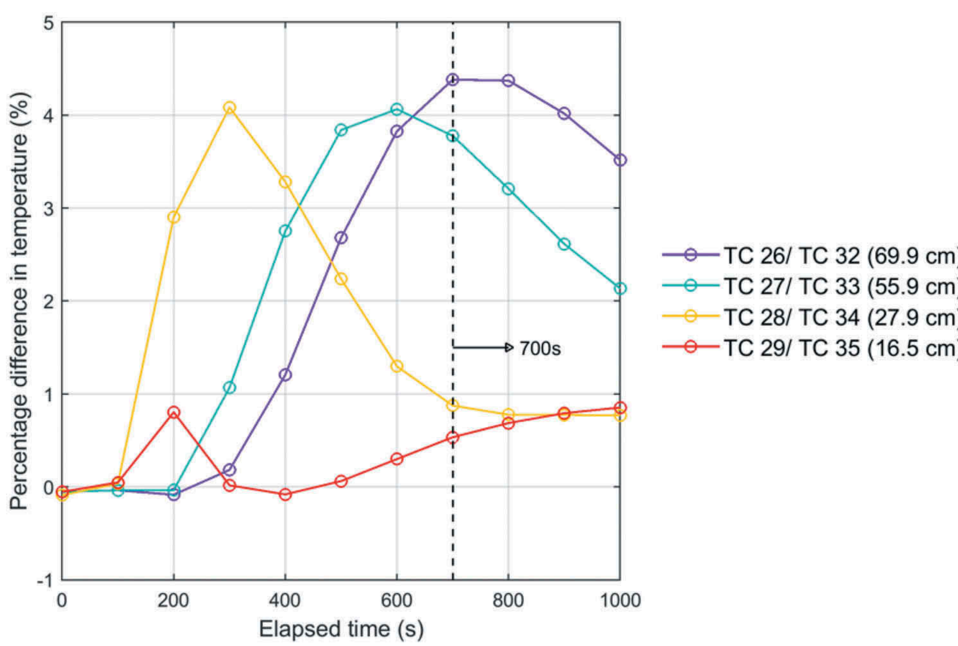

Fig. 7. Percentage difference between predictions and experiments in test 4.

thermal conductivity could become several times larger than that in a static state. The correlation of Shih et al.[16] was used in the first place, according to which $k_{sf} = k_c$. However, this empirical correlation might not be applicable to the 1-D thermal stratification model because it was established by considering the impinging jet and the ambient fluid as a mixture, while the 1-D thermal stratification model focused on the ambient fluid and considered the impinging jet as a heat source. The boundaries of the regimes and the coefficients of the correlations may

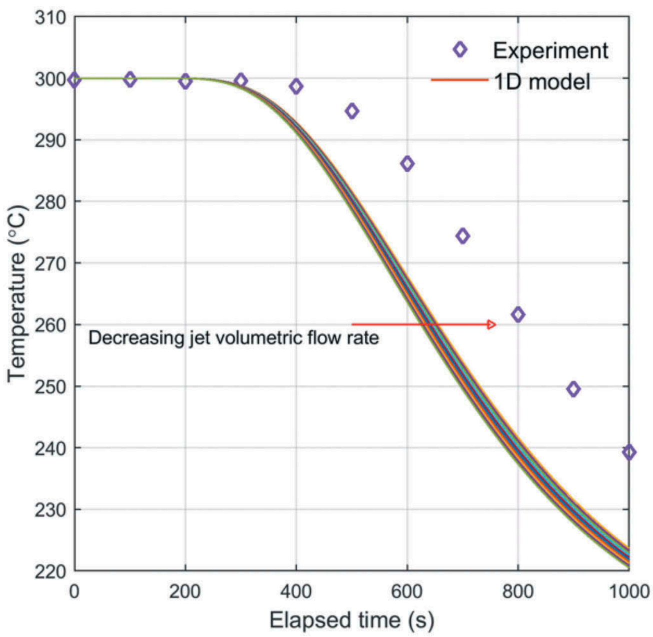

Fig. 8. Ambient temperature prediction at TC 26/TC 32 (69.9 cm) with various perturbed impinging jet flow rates in test 4.

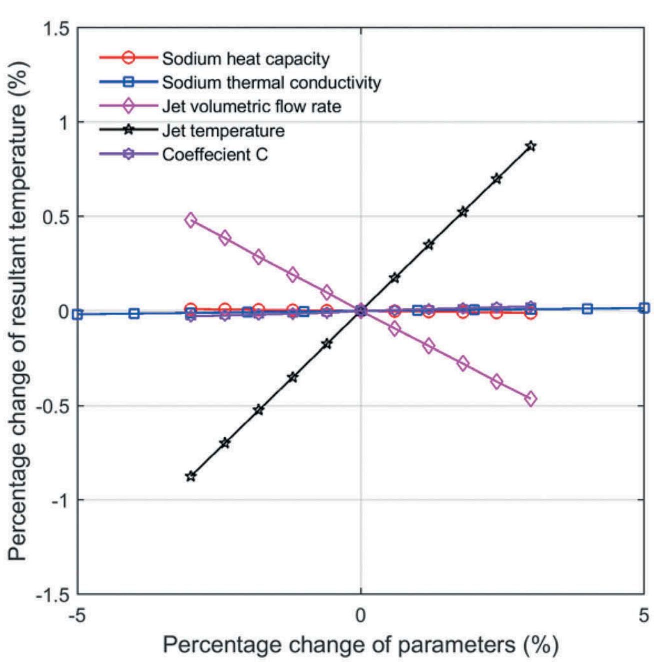

Fig. 9. Temperature percentage change due to different parameters at 700 s in test 4.

therefore be different. In Sec. IV we will determine the optimal coefficients a and b such that the relationship of k_{sf} and k_c in a form of

$$k_{sf} = a\left(\frac{Re_\tau}{Ri}\right)^b \cdot k_c \ , \tag{4}$$

can minimize the discrepancy between the 1-D prediction and the experimental data. The advanced inverse UQ process assisted us in achieving this goal.

IV. INVERSE UQ ON TURBULENCE-ENHANCED SODIUM THERMAL CONDUCTIVITY

Inverse UQ is a Bayesian-inference-based data-assimilation method. Compared to conventional parameter-calibration methods, including those based on linear least squares, inverse UQ has the advantage of being able to simultaneously determine the point estimates that minimize the mismatches between the predictions and experimental measurements while quantifying the associated parameter uncertainties. In the following subsections, the inverse UQ method is briefly introduced, and the application of the inverse UQ method to the 1-D thermal stratification model is then detailed.

IV.A. Methodology of the Inverse UQ Process

The philosophy of the inverse UQ method is briefly introduced in this section because detailed and in-depth discussions of the formulation of the inverse UQ problem have already been given in numerous existing publications.[18,19] According to the Bayesian theory, the posterior PDF can be expressed as a product of the prior PDF and the likelihood function:

$$p(\boldsymbol{\theta}^*|\boldsymbol{y}^E,\boldsymbol{y}^M) \propto p(\boldsymbol{\theta}^*) \times \frac{1}{\sqrt{|\boldsymbol{\Sigma}|}} \times \exp\left[-\frac{1}{2}\left[\boldsymbol{y}^E - \boldsymbol{y}^M - \boldsymbol{\delta}\right]^T \boldsymbol{\Sigma}^{-1}\left[\boldsymbol{y}^E - \boldsymbol{y}^M - \boldsymbol{\delta}\right]\right] , \tag{5}$$

where $p(\boldsymbol{\theta}^*)$ denotes the prior PDF, and $p(\boldsymbol{\theta}^*|\boldsymbol{y}^E,\boldsymbol{y}^M)$ denotes the posterior PDF, which is the Bayesian solution to the inverse UQ problem. These two PDFs, respectively, represent the degrees of the belief of $\boldsymbol{\theta}^*$, which are the true values of the calibration parameters before and after observing the experimental data $\boldsymbol{y}^E(\boldsymbol{x})$ where $\boldsymbol{x}$ represents the design variables (such as initial and boundary conditions). In the current study, the calibration variables $\boldsymbol{\theta}$ included parameters a and b in Eq. (4), as well as C in Eq. (3). The design variables $\boldsymbol{x}$ included the initial ambient fluid temperature, jet temperature, and jet volumetric flow rate, etc. $\boldsymbol{y}^M(\boldsymbol{x})$ is the computational prediction of the 1-D thermal stratification model. $\boldsymbol{\delta}(\boldsymbol{x})$is the model discrepancy caused by the missing or insufficient underlying physics of the 1-D model, as well as numerical approximations. In the current study, $\boldsymbol{\delta}(\boldsymbol{x})$is mainly caused by the errors introduced by the approximations of the 1-D thermal stratification model, including the assumption of a uniform distributed impinging jet dispersion rate and other simplifications made during its derivation.

The symbol $\boldsymbol{\Sigma}$ in Eq. (5) denotes the likelihood covariance matrix, whose diagonal entries represent the variance of each error component with the off-diagonal entries representing their covariance. $\boldsymbol{\Sigma}$ consists of several sources of uncertainties, including $\boldsymbol{\Sigma}_{\text{exp}}$, $\boldsymbol{\Sigma}_{\text{bias}}$, and $\boldsymbol{\Sigma}_{\text{code}}$:

$$\boldsymbol{\Sigma} = \boldsymbol{\Sigma}_{\text{exp}} + \boldsymbol{\Sigma}_{\text{bias}} + \boldsymbol{\Sigma}_{\text{code}} \,, \tag{6}$$

where $\boldsymbol{\Sigma}_{\text{exp}}$ is the covariance matrix of experiment uncertainty due to measurement noise. In the current study, the experiment uncertainty was associated with the ambient fluid temperature measurement and was assumed to be independent and identically normally distributed. We considered that the TCs had no systematic bias, and the measurement uncertainty was 2%. $\boldsymbol{\Sigma}_{\text{bias}}$ is the covariance matrix of model discrepancy $\boldsymbol{\delta}(\boldsymbol{x})$, the existence of which has been proven in our previous publication.[11] $\boldsymbol{\delta}(\boldsymbol{x})$ is usually described by establishing a Gaussian process (GP) model.[20,21] Because of the lack of the experimental data, we were not able to establish the GP model for $\boldsymbol{\delta}(\boldsymbol{x})$, and therefore ignored this term in this study.

The posterior PDF formulation shown in Eq. (5) is nonstandard and not normalized, and cannot be directly used to generate samples like any conventional distributions. Therefore, the MCMC (Ref. 22) sampling method is often used to explore the posterior function numerically by generating samples that follow a distribution proportional to the posterior PDF. MCMC requires a sufficiently large number of samples to fully explore the posteriors, which makes the calculation computationally expensive. In order to reduce the computational burden, many methodologies are usually employed to establish surrogate models for $\boldsymbol{y}^M(\boldsymbol{x})$ during the MCMC sampling process. Typical examples of the surrogate models include GP modeling, sparse grid stochastic collocation, and polynomial chaos expansion, etc. However, the use of the surrogate model inevitably introduces additional uncertainties into the resultant posteriors calculated through the inverse UQ process, and $\boldsymbol{\Sigma}_{\text{code}}$ in Eq. (6) is the corresponding covariance matrix representing those uncertainties. In the current study, each full 1-D model calculation took less than 1 s. Because of the acceptable computational expense required, we decided not to use a surrogate model to avoid the associated uncertainties. Given the considerations discussed here, in the current study Eqs. (5) and (6) are simplified to

$$p\left(\boldsymbol{\theta}^*|\boldsymbol{y}^E,\boldsymbol{y}^M\right) \propto p(\boldsymbol{\theta}^*)\cdot\frac{1}{\sqrt{|\boldsymbol{\Sigma}|}} \times \exp\left[-\frac{1}{2}\left[\boldsymbol{y}^E-\boldsymbol{y}^M\right]^T\boldsymbol{\Sigma}^{-1}\left[\boldsymbol{y}^E-\boldsymbol{y}^M\right]\right] \,, \tag{7}$$

and

$$\boldsymbol{\Sigma} = \boldsymbol{\Sigma}_{\text{exp}} \,. \tag{8}$$

IV.B. Subcase I with UIS Installed

As shown in Table I, tests 1, 2, and 3 correspond to the experiments with UIS installed in the tank. The ambient fluid temperature was measured continuously in all the experiments. The temperature measurements at 11 elapsed times in test 1 and 3, and at 8 elapsed times in test 2 were used to cover the entire transient of the experiments, which can be clearly viewed in Figs. 13, 14, and 15.

In this subcase, data from tests 1 and 2 were used for the inverse UQ process, and data from test 3 were used for the validation of the resultant posteriors. Noninformative uniform priors of the parameters, including $a \in [0, 20]$ and $b \in [0, 1]$, were used to reflect our ignorance of both parameters. In total, 100 000 samples were generated for the inverse UQ study, which cost about 14 h of a single processor unit. The number of iterations used was chosen to ensure the convergence of each parameter. The first 10 000 samples were discarded for burn-in, so that the sample points generated before the convergence would not pollute the estimation of the posteriors. Then, every 20th sample was kept from the remainder for thinning the chain to reduce autocorrelation among the samples, which left us with 4500 samples. The trace plots of the 4500 samples for a and b are shown in Fig. 10. Due to the nature of the inverse UQ method, the coefficients a and b determined were not the point estimates, but the probability distributions. We can therefore see oscillations in the traces of a and b around their nominal values. The resultant posteriors of both parameters for subcase I are shown in Fig. 11. Gaussian distributions $a{\sim}N(8.05,\ 0.90)$ and $b{\sim}N\left(0.33,\ 3\times10^{-3}\right)$ were fitted to the posteriors of both coefficients, which were accepted by the Kolmogorov-Smirnov test[23] at the 5% significance

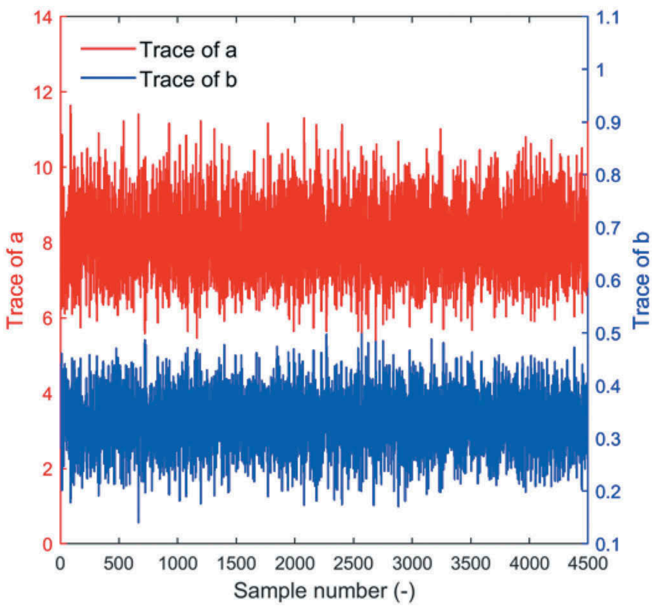

Fig. 10. Trace plots for parameters a and b for subcase I.

level. This suggested that the optimal value of a should be 8.05 with an uncertainty of ±0.95, and the optimal value of b should be 0.33 with an uncertainty of ±0.055. Figure 12 shows good agreement between the empirical cumulative distribution functions (CDFs) of both coefficients and the CDF of the fitted Gaussian distributions, which again confirmed the fit of the distributions to the posteriors to be reasonable.

Comparisons of the 1-D thermal stratification prediction before and after the inverse UQ process with the experimental data are shown in Figs. 13, 14, and 15 for tests 1, 2, and 3, respectively. The maximum and the averaged values of the magnitude (absolute value) of the discrepancies between the 1-D predictions and the experimental measurement are summarized in Table III. Because tests 1 and 2 were used during the inverse UQ process, the resultant 1-D predictions for those two test conditions had a trend that was much more compatible with that of the experimental data, and the magnitude of the discrepancies was largely decreased. However, due to the missing or insufficient physics of the 1-D model, the prediction was not able to perfectly match the experimental data even after the inverse UQ process. When test 3 was considered, the inverse UQ process reduced the magnitude of the discrepancies between the 1-D prediction and the experimental data, but not as prominently as for the other two test conditions. This again revealed the missing or insufficient physics of the 1-D model. However, the fact that the trend of 1-D prediction for test 3 was improved, as well as the other two test conditions, proved the use of the inverse UQ process to be reasonable.

IV.C. Subcase II with No UIS Installed

As shown in Table I, tests 4 through 9 are experiments with no UIS installed in the tank. Temperature measurements at 11 elapsed times in tests 4 through 7, and at five elapsed times in tests 8 and 9 were used such that the entire transient of the experiments was covered, as shown in Figs. 19 through 24.

In this subcase, tests 5 and 6 were used to perform the inverse UQ process, while tests 4, 7, 8, and 9 were used for the validation of the resultant posteriors. Noninformative uniform priors of the parameters, including $a \in [0, 50]$ and $b \in [-2, 2]$, were used to reflect our ignorance of both parameters. Similar to subcase I, 100 000 samples in total were generated for the inverse UQ study, which again cost about 14 h of a single processor unit. The number of iterations used was chosen to

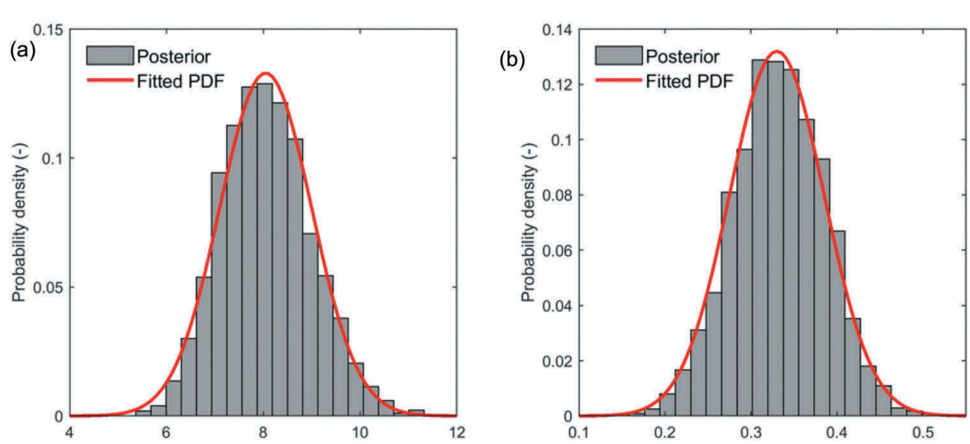

Fig. 11. Posteriors of (a) a and (b) b explored by MCMC samples and the fitted Gaussian distributions for subcase I.

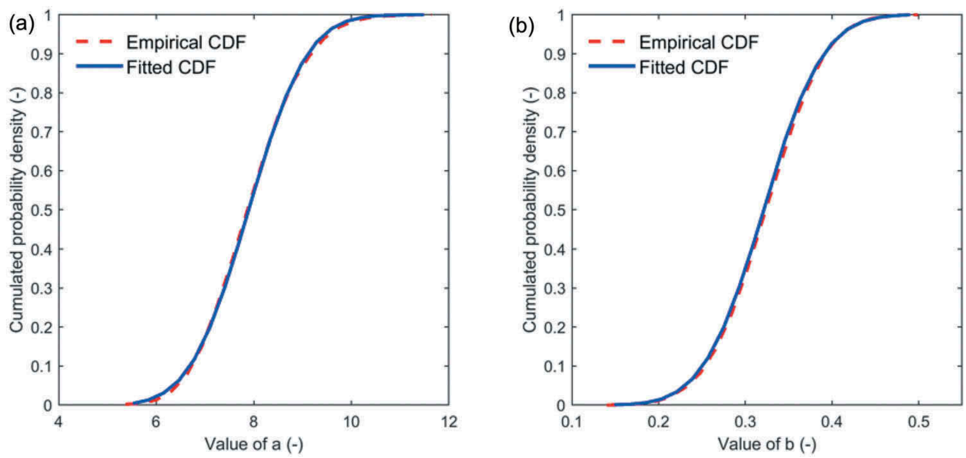

Fig. 12. Comparison of empirical CDFs from MCMC samples and fitted CDFs of (a) a and (b) b for subcase I.

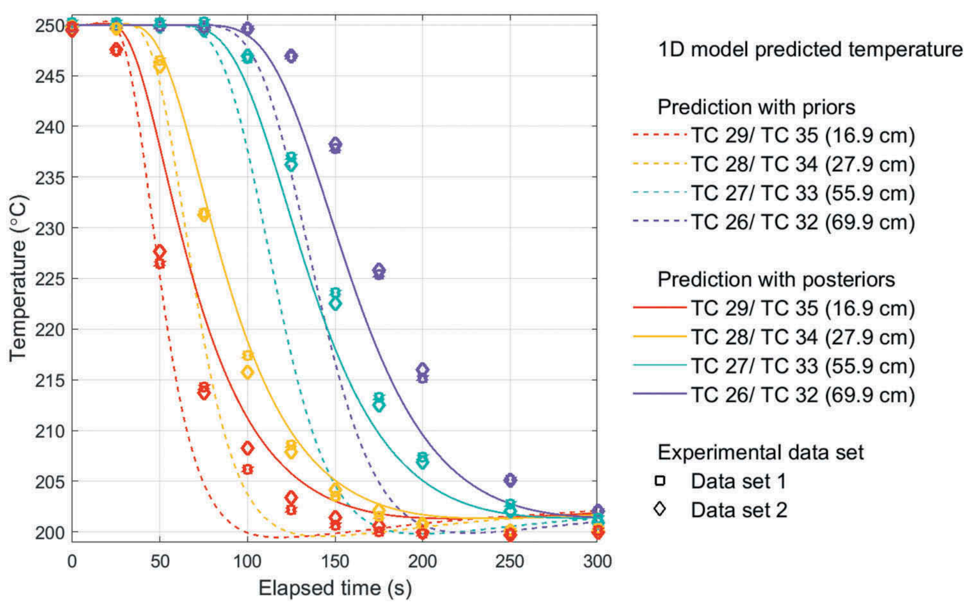

Fig. 13. Comparison of the 1-D thermal stratification prediction before and after the inverse UQ process with the experimental data sets for test 1.

ensure the convergence of each parameter selected. The first 10 000 samples were discarded during the posterior exploration for burn-in so that the sample points generated before the convergence would not pollute the estimation of the posteriors. Then, every 20th sample was kept from the remainder for thinning of the chain to reduce autocorrelation among the samples, which left us with 4500 samples. The trace plots of the 4500 samples for a and b are shown in Fig. 16, and the resultant posteriors of both parameters for subcase II are shown in Fig. 17. Gamma distribution $\Gamma(5.4,\ 2.2)$ was fitted to coefficient a, while Gaussian distribution $N(0.13,\ 0.02)$ was fitted to coefficient b. This suggested that the optimal value of a should be 9.7 with an uncertainty of ±5.1, and the optimal value of b should be 0.13 with an uncertainty of ±0.14. Both fitted distributions were accepted by the Kolmogorov-Smirnov test at the 5% significance level. Figure 18 shows good agreement between the empirical CDFs of both coefficients and the CDF of the fitted distributions, which again confirmed the fit of the distributions to the posteriors to be reasonable.

Comparisons of the 1-D thermal stratification prediction before and after the inverse UQ process with the experimental data are shown in Figs. 19 through 24 for tests 4 through 9, respectively. The maximum and the averaged values of the magnitude (absolute value) of discrepancies between the 1-D predictions and the experimental measurement are summarized in Table IV. For the

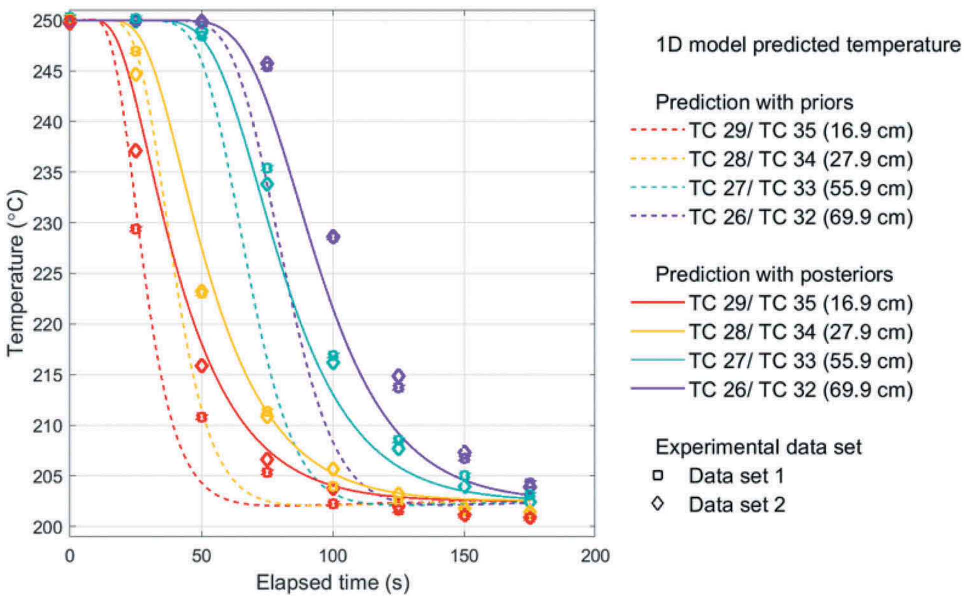

Fig. 14. Comparison of the 1-D thermal stratification prediction before and after the inverse UQ process with the experimental data for test 2.

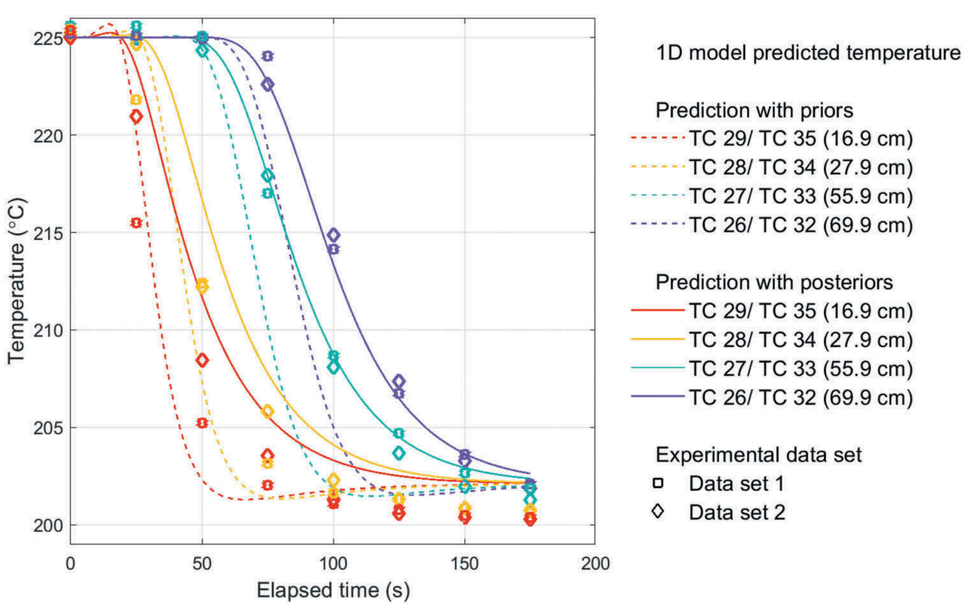

Fig. 15. Comparison of the 1-D thermal stratification prediction before and after the inverse UQ process with the experimental data for test 3.

same reason as stated for subcase I, the resultant 1-D predictions for tests 4 through 7 had a trend that was much more compatible with that of the experimental data, and the magnitude of the discrepancies was largely decreased. However, the improvement of the 1-D model brought by the new thermal conductivity correlation became less prominent in tests 8 and 9, when the impinging jet mass flow rate became higher. This is because with a large jet length, the ambient fluid at different axial locations was directly cooled by the impinging jet, and its temperature change through heat conduction became minor.

The ratios of the turbulent Re_τ to the Ri of the nine test conditions are summarized in Table V together with the k_{sf}/k_c ratios obtained through the inverse UQ process. Because of the large difference of the Re_τ/Ri ratios, tests

TABLE III

Magnitude of the Maximum Prediction Error for Subcase I

Test Number	Maximum Error Before Inverse UQ (°C)	Maximum Error After Inverse UQ (°C)	Average Error Before Inverse UQ (°C)	Average Error After Inverse UQ (°C)
1	21.0	12.0	5.0	2.5
2	20.0	13.5	4.5	2.0
3	9.5	8.5	2.0	1.5

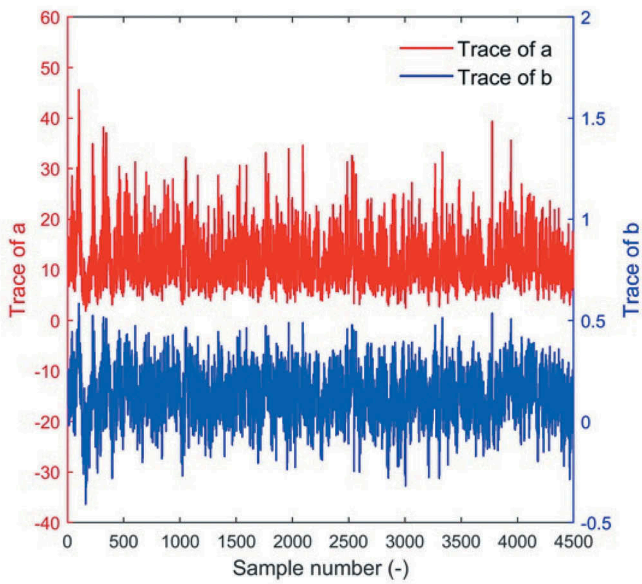

Fig. 16. Trace plots for a and b for subcase II.

1, 2, and 3 and tests 4 through 7 were classified into two different mixing regimes. Both coefficients a and b obtained for these two mixing regimes were different. However, the classification of tests 8 and 9 were unclear because of the minor impact of thermal conductivity on temperature distribution in these two test conditions.

Besides the correlation for turbulence-enhanced sodium thermal conductivity, the highly simplified jet model employed in the initial 1-D model was another source of deficiencies. For test conditions with no UIS installed and with large impinging jet flow rates, including tests 8 and 9, the new thermal conductivity correlation had a minor impact on the 1-D predictions, whereas a better jet model is expected to significantly improve the performance of the 1-D thermal stratification model.

V. SUMMARY AND CONCLUSIONS

A fast-running 1-D system-level model was previously developed by our research group to predict the thermal stratification phenomenon in the upper plenum of a pool-type SFR (Refs. 11 and 12). The 1-D model had reasonable performance, but nonnegligible discrepancies between the 1-D predictions and the experimental temperature measurements were observed.[11] In this paper, we first conducted a forward UQ study to the previously

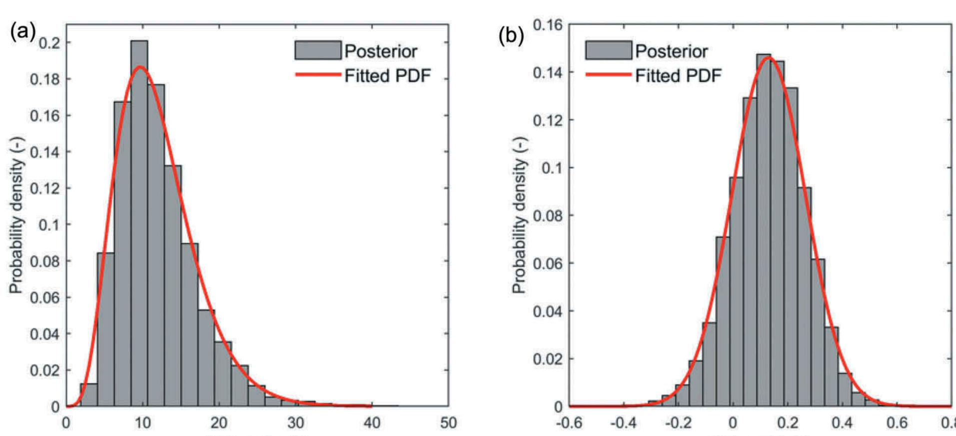

Fig. 17. Posteriors of (a) a and (b) b explored by MCMC samples and the fitted distributions for subcase II.

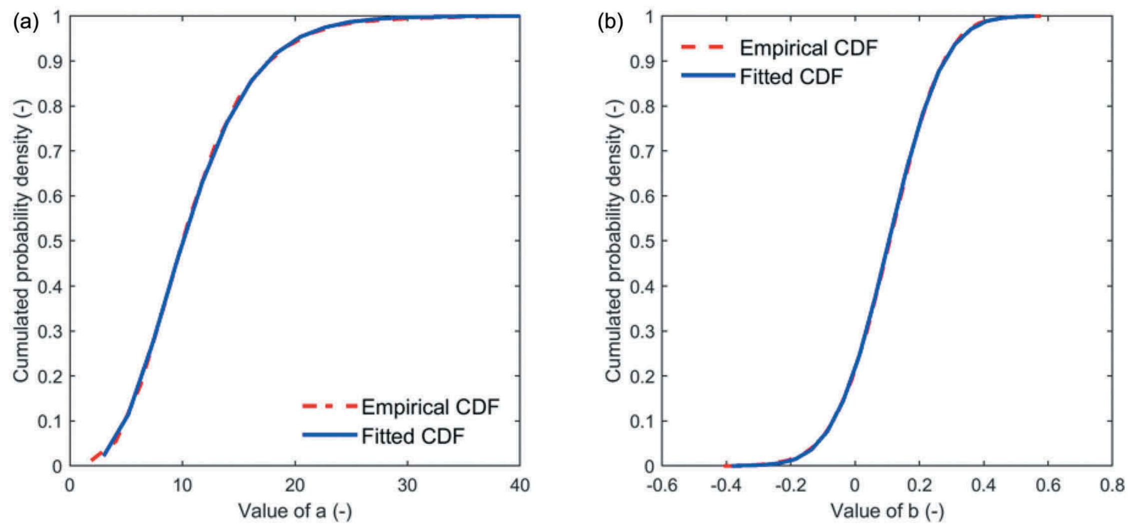

Fig. 18. Comparison of empirical CDFs from MCMC samples and fitted CDFs of (a) a and (b) b for subcase II.

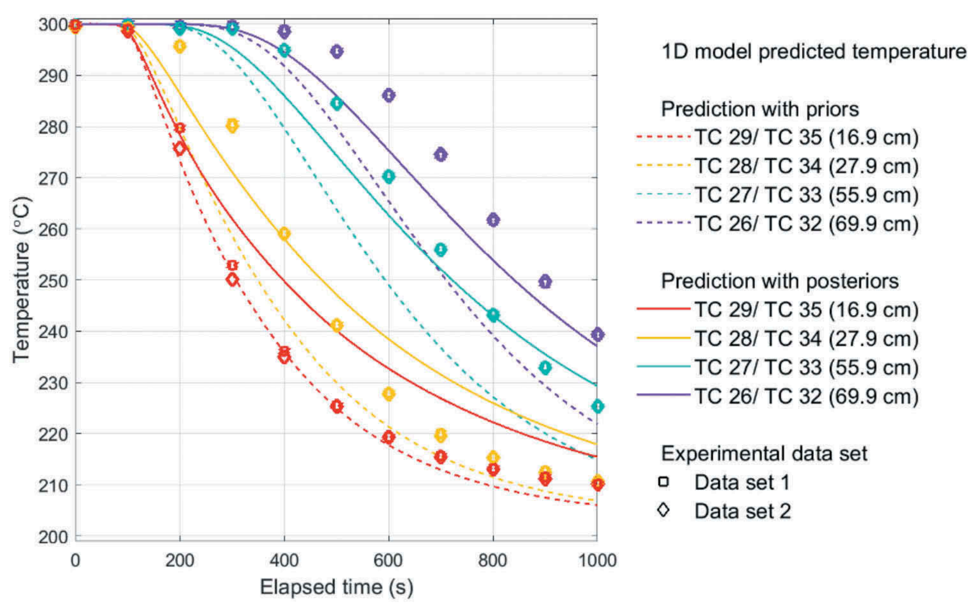

Fig. 19. Comparison of the 1-D thermal stratification prediction before and after the inverse UQ process with the experimental data for test 4.

developed 1-D thermal stratification model to identify the uncertainty resources of the observed discrepancies between the 1-D predictions and the experimental measurements. Two key input parameters (jet temperature and jet volumetric flow rate) and two thermal-hydraulic system parameters (sodium heat capacity and thermal conductivity) were considered in conjunction with the coefficient C of the jet model. For both subcases investigated in this study (the ones with and without UIS installed), the percentage change of the temperature of interest caused by the uncertainties of inlet temperature and inlet volumetric flow rate was more significant. However, these uncertainties could not compensate for the observed temperature discrepancies between the 1-D predictions and the experimental measurements. For subcase II, the uncertainty of the coefficient C caused much smaller uncertainty in the temperature of interest compared to the jet temperature and the jet volumetric flow rate. On the other hand, large changes would be introduced by the turbulence-enhanced thermal

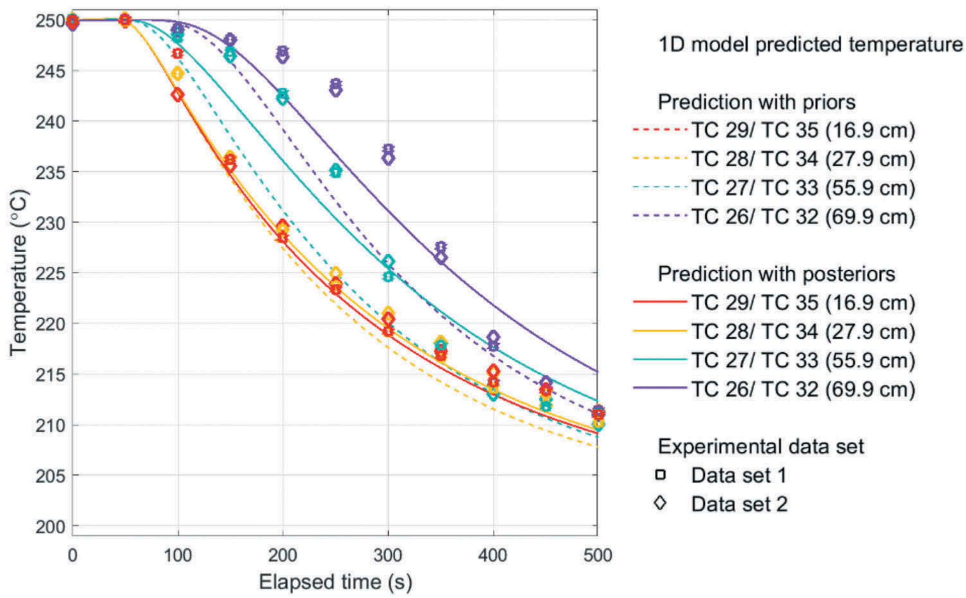

Fig. 20. Comparison of the 1-D thermal stratification prediction before and after the inverse UQ process with the experimental data for test 5.

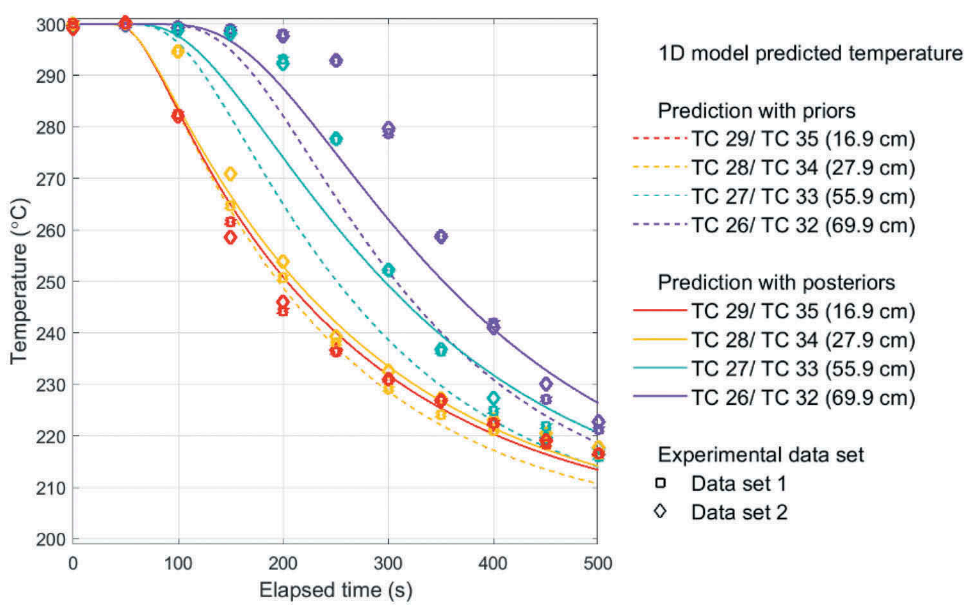

Fig. 21. Comparison of the 1-D thermal stratification prediction before and after the inverse UQ process with the experimental data for test 6.

conductivity of sodium when the ambient flow is classified to different flow regimes and further impacts the 1-D prediction. This indicated that the correlation, developed by Shih et al. for the estimation ofk_{sf}, needed modifications to be applicable to our 1-D thermal stratification model. The coefficients and the boundaries of the mixing regimes in this study were different from those of Shih et al.'s correlation because we focused on the ambient fluid and considered the impinging jet as a heat source in our 1-D thermal stratification model, while Shih et al. established their correlation by treating the impinging jet and the ambient fluid as a mixture.

We then proceeded to develop an improved correlation to be used for the k_{sf} estimation in the

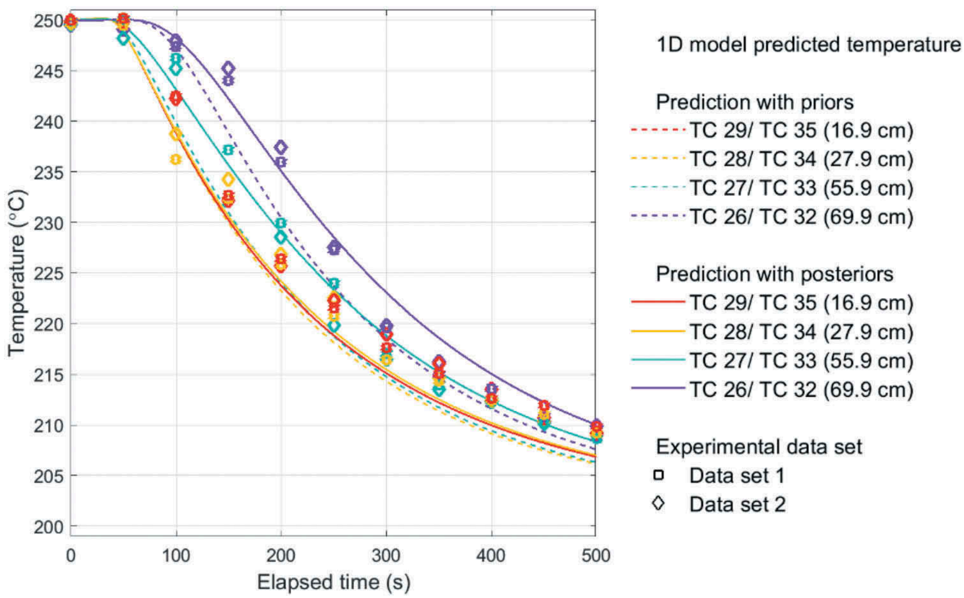

Fig. 22. Comparison of the 1-D thermal stratification prediction before and after the inverse UQ process with the experimental data for test 7.

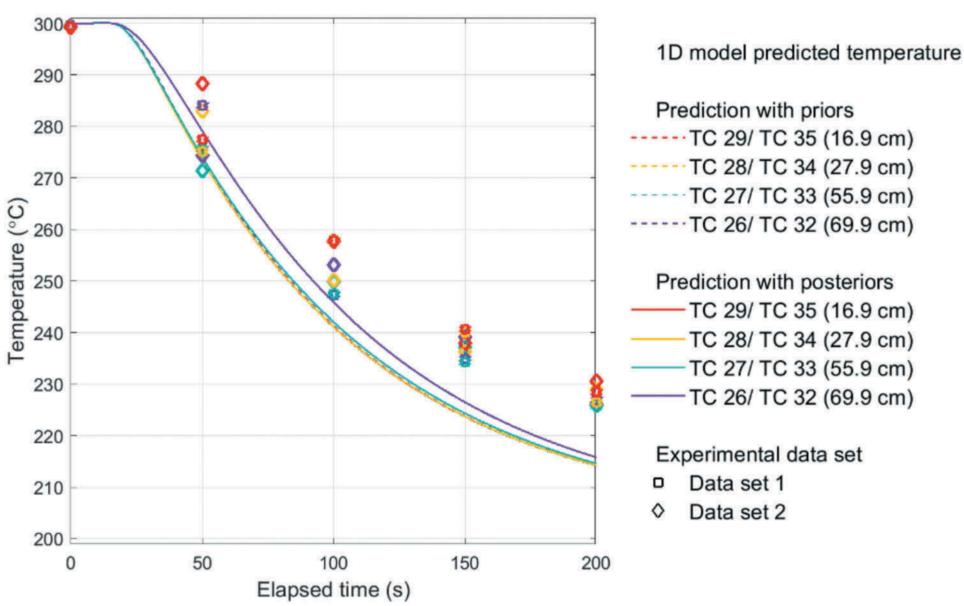

Fig. 23. Comparison of the 1-D thermal stratification prediction before and after the inverse UQ process with the experimental data for test 8.

1-D thermal stratification model by using an efficient data assimilation approach: the Bayesian-inference-based inverse UQ process. We determined a combination of the coefficients *a* and *b* for the modeling of the turbulence-enhance sodium thermal conductivity in both subcases to minimize the discrepancies between the 1-D predictions and the experimental measurements. We also quantified the uncertainties associated with these two coefficients in the same process. Among the nine experiments performed, we used four of them for the inverse UQ process and the other five for the validation.

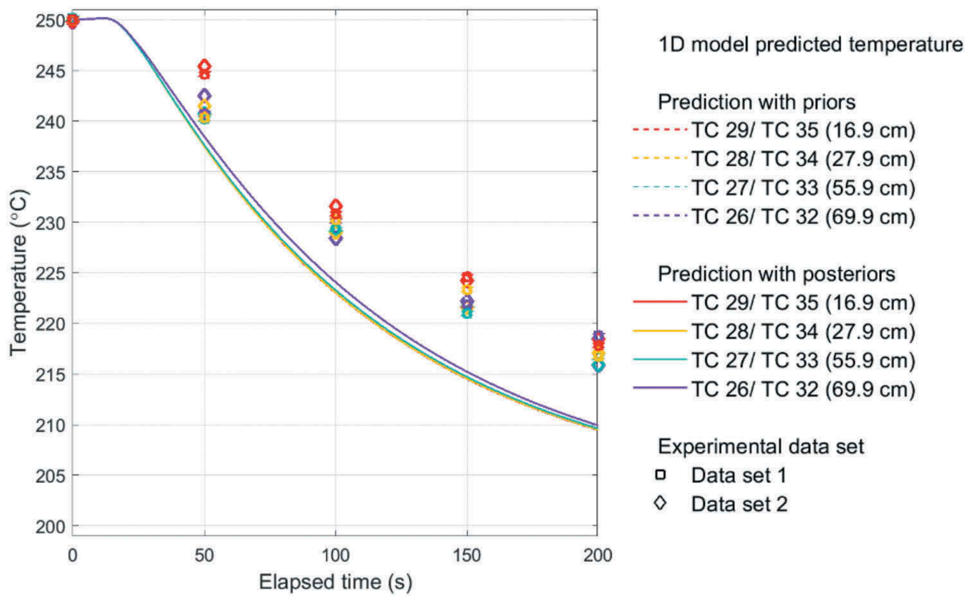

Fig. 24. Comparison of the 1-D thermal stratification prediction before and after the inverse UQ process with the experimental data for test 9.

TABLE IV

Magnitude of the Maximum Prediction Error for Subcase II

Test Number	Maximum Error Before Inverse UQ (°C)	Maximum Error After Inverse UQ (°C)	Average Error Before Inverse UQ (°C)	Average Error After Inverse UQ (°C)
4	23.0	15.0	8.0	6.0
5	11.5	7.0	3.0	2.0
6	28.0	19.0	6.5	4.5
7	7.0	3.5	2.5	1.5
8	16.5	16.5	8.5	8.0
9	10.0	10.0	5.5	5.0

TABLE V

Summary of Re_τ/Ri Ratios and the Resultant k_{sf}/k_c Ratios

Test Number	Re_τ/Ri	Correlation for k_{sf}/k_c Ratio Through Inverse UQ	k_{sf}/k_c
1	4.55	$8.1\left(\frac{Re_\tau}{Ri}\right)^{0.33}$	13.3
2	21.1		22.0
3	42.7		27.8
4	0.01	$9.7\left(\frac{Re_\tau}{Ri}\right)^{0.13}$	5.0
5	0.06		6.7
6	0.04		6.3
7	0.10		7.2
8	0.76		9.3
9	1.41		10.1

Based on the results of the inverse UQ process for the enhanced model development, we extend the following conclusions. The inverse UQ showed good capability of determining the calibration parameters and providing the associated uncertainties in the current study. The 1-D thermal stratification model was substantially improved by using the optimal posteriors of the investigated coefficients determined through the inverse UQ process. By using the coefficients a and b determined through the inverse UQ process, the 1-D predictions for most of the test conditions showed a trend that better matched the experimental data. Moreover, the average discrepancy between the 1-D prediction and the experimental measurements was reduced by 25% to 50% for the experiments with the UIS installed, and by 25% to 33% for the experiments with no UIS installed (except for tests 8 and 9). This demonstrated the usefulness and the necessity of investigating these two parameters. However, the 1-D model was not able to make predictions that perfectly matched the experimental data, even for the test conditions used for the inverse UQ process. This revealed the existence of other missing or insufficient physics of the model. Besides the correlation for turbulence-enhanced sodium thermal conductivity, the highly simplified jet model employed in the initial 1-D model could be another source of deficiencies. For tests 8 and 9, conditions with no UIS installed in the tank and large impinging jet flow rates, the new thermal conductivity correlation had a minor impact on the 1-D predictions. A better jet model is expected to further improve the performance of the 1-D thermal stratification model for these test conditions, and will be the focus of our future research.

Acknowledgments

The authors are grateful to the two anonymous reviewers of this manuscript for their constructive comments and suggestions.

ORCID

Cihang Lu http://orcid.org/0000-0002-6385-6338
Zeyun Wu http://orcid.org/0000-0002-6114-0352
Xu Wu http://orcid.org/0000-0002-0436-5969

References

1. Z. WU et al., "A Status Review on the Thermal Stratification Modeling Methods for Sodium-Cooled Fast Reactors," *Prog. Nucl. Energy*, **125**, 103369 (2020); https://doi.org/10.1016/j.pnucene.2020.103369.

2. M. AZARIAN et al., "Sodium Thermal-Hydraulics in the Pool LMFBR Primary Vessel," *Nucl. Eng. Des.*, **124**, *3*, 417 (1990); https://doi.org/10.1016/0029-5493(90)90305-H.

3. B. WARD, J. CLARK, and H. BINDRA, "Thermal Stratification in Liquid Metal Pools Under Influence of Penetrating Colder Jets," *Exp. Therm Fluid Sci.*, **103**, 118 (2019); https://doi.org/10.1016/j.expthermflusci.2018.12.030.

4. B. WARD et al., "Scaling of Thermal Stratification or Mixing in Outlet Plena of SFRs," *Ann. Nucl. Energy*, **112**, 431 (2018); https://doi.org/10.1016/j.anucene.2017.10.032.

5. D. PIALLA et al., "Overview of the System Alone and System/CFD Coupled Calculations of the PHENIX Natural Circulation Test Within the THINS Project," *Nucl. Eng. Des.*, **290**, 78 (2015); https://doi.org/10.1016/j.nucengdes.2014.12.006.

6. F. YAMADA et al., "Development of Natural Circulation Analytical Model in Super-COPD Code and Evaluation of Core Cooling Capability in Monju During a Station Blackout," *Nucl. Tech.*, **188**, *3*, 292 (2014); https://doi.org/10.13182/NT13-56.

7. H. ZHAO and P. F. PETERSON, "One-Dimensional Analysis of Thermal Stratification in AHTR and SFR Coolant Pools," INL/CON-06-12026, Idaho National Laboratory (2007).

8. M. SHIBAHARA, T. TAKATA, and A. YAMAGUCHI, "Numerical Simulation of Dynamic Flow Structure and Thermal Stratification Phenomena in LMFBR," *Proc. 19th Int. Conf. on Nuclear Engineering (ICONE-19)*, Osaka University, Japan, October 24–25, 2011.

9. T. SOFU, J. THOMAS, and T. FANNING, "Analysis of Thermal Stratification in the Upper Plenum of the Monju Reactor Vessel Using a Simplified Model," presented at the 2nd RCM of the IAEA CRP on Benchmark Analysis of Monju Natural Convection, Marcoule, France, October 12–14, 2009.

10. S. K. CHOI et al., "Numerical Analysis of Thermal Stratification in the Upper Plenum of the Monju Fast Reactor," *Nucl. Eng. Tech.*, **45**, *2*, 191 (2013); https://doi.org/10.5516/NET.02.2012.050.

11. C. LU et al., "An Efficient 1-D Thermal Stratification Model for Pool-Type Sodium-Cooled Fast Reactors," *Nucl. Technol.*; https://doi.org/10.1080/00295450.2020.1719799.

12. C. LU et al., "Thermal Stratification Analysis for Sodium-Cooled Fast Reactors: Development of the 1-D System Model," *Trans. Am. Nucl. Soc.*, **121**, 1703 (2019).

13. D. LI, X. LIU, and Y. YANG, "Investigation of Uncertainty Quantification Method for BE Models Using MCMC

Approach and Application to Assessment with FEBA Data," *Ann. Nucl. Energy*, **107**, 62 (2017); https://doi.org/10.1016/j.anucene.2017.04.020.

14. J. ZHANG et al., "Development of a Pragmatic Approach to Model Input Uncertainty Quantification for BEPU Applications," *Nucl. Technol.*, **205**, *1–2*, 140 (2019); https://doi.org/10.1080/00295450.2018.1516055.
15. J. SCHNEIDER et al., "Thermal Stratification Analysis for Sodium Fast Reactors" *Proc. Int. Congress on Advances in Nuclear Power Plants (ICAPP)*, Charlotte, North Carolina, April 9–11, 2018.
16. L. H. SHIH et al., "Parameterization of Turbulent Fluxes and Scales Using Homogeneous Sheared Stably Stratified Turbulence Simulations," *J. Fluid Mech.*, **525**, 193 (2005); https://doi.org/10.1017/S0022112004002587.
17. J. K. FINK and L. LEIBOWITZ, "Thermodynamic and Transport Properties of Sodium Liquid and Vapor," ANL/RE-95/2, Argonne National Laboratory (1995).
18. X. WU, T. KOZLOWSKI, and H. MEIDANI, "Kriging-Based Inverse Uncertainty Quantification of Nuclear Fuel Performance Code BISON Fission Gas Release Model Using Time Series Measurement Data," *Reliab. Eng. Syst. Saf.*, **169**, 422 (2018); https://doi.org/10.1016/j.ress.2017.09.029.
19. X. WU et al., "Inverse Uncertainty Quantification Using the Modular Bayesian Approach Based on Gaussian Process. Part 1: Theory," *Nucl. Eng. Des.*, **335**, 339 (2018); https://doi.org/10.1016/j.nucengdes.2018.06.004.
20. X. WU et al., "Inverse Uncertainty Quantification Using the Modular Bayesian Approach Based on Gaussian Process, Part 2: Application to TRACE," *Nucl. Eng. Des.*, **335**, 417 (2018); https://doi.org/10.1016/j.nucengdes.2018.06.003.
21. D. C. WICAKSONO, O. ZERKAK, and A. PAUTZ, "Bayesian Calibration of Thermal-Hydraulics Model with Time-Dependent Output," *Proc. NUTHOS-11*, Gyeongju, Korea, October 9–13, 2016.
22. W. R. GILKS, S. RICHARDSON, and D. SPIEGELHALTER, *Markov Chain Monte Carlo in Practice*, CRC Press (1995).
23. F. J. MASSEY, "The Kolmogorov-Smirnov Test for Goodness of Fit," *J. Am. Stat. Assoc.*, **46**, *253*, 68 (1951); https://doi.org/10.1080/01621459.1951.10500769.